Progress In Electromagnetics Research C, Vol. 138, 145–159, 2023

Three-Dimensional Imaging of Target Based on Time-Domain Sparse Representation of Multi-View SAR Data

Jinrong Zhong[1], Xing Zhang[2, *], and Shengqi Liu[3]

Abstract—Three-dimension (3-D) images provide additional information of targets for automatic target recognition (ATR) and 3D scattering model generation. Methods based on sparse representations can reconstruct extreme resolution 3D images from sparse measurements, but suffer from the huge dimension of separable dictionaries. This paper presents a time-domain sparse representation method for 3-D target imaging from multi-view synthetic aperture radar (SAR) data, including a basic method and two improved ones. The time-domain framework uses time-domain responses to build a separable dictionary and a sparse representation model. In the time-domain framework, the basic approach is to transform the dictionary into a rather sparse matrix via a low-energy threshold that shrinks the spatial region of the 3D imaging based on multi-aspect 2D images. By exploiting the properties of multi-aspect SAR data in the time domain, one modification makes the sparse representation model more compact, leading to a reduction in dimensionality, and another additional modification splits a high-dimensional large-scale model into a set of very low-dimensional small-scale models. They overcome the curse of dimensionality and improve the efficiency of sparse representation-based 3D imaging to varying degrees. Experimental results show the effectiveness and great efficiency of the proposed method.

1. INTRODUCTION

Synthetic aperture radar (SAR) is an effective means of ground observation. Three-dimensional (3-D) imaging of target can provide significant and intuitive characteristics for reconnaissance and automatic target recognition (ATR) [1–7], and is an essential method in generating the scattering model of target [8–10]. It is attractive to generate 3-D images of target from multi-aspect SAR measurements [11–13]. Fourier imaging methods require radar to collect data over densely sampled points in both azimuth and elevation [14]. In recent years, sparse-representation based 3-D radar imaging methods have been developed and show advantages and super performance on sparsely collections [15–21]. However, the huge dimension of separable dictionaries, as well as the costly computation to solve them, is an obstacle for sparse representation-based methods. Efficient and faster methods are always sought [22–25].

In this paper, we propose a time-domain sparse representation framework for 3D imaging from multi-aspect SAR measurements, whereas most existing sparse methods work in the frequency domain. In the time-domain framework, we present a basic 3D imaging method and two improvements. The basic approach uses multi-aspect 2-D SAR images to exclude 3-D regions, where no scattering center is located, and constructs a dictionary for candidate locations only. It leads to a reduction in the row dimension of the dictionary. Then, the low-energy region of the time-domain dictionary is truncated to make it a fairly sparse matrix, which significantly saves storage space. Exploiting the property that the energy of a 2D SAR image is congested in several narrow regions, the first improved method reduces the column dimension of the dictionary. It transforms the sparse representation model in the

Received 10 March 2023, Accepted 13 September 2023, Scheduled 22 October 2023
* Corresponding author: Xing Zhang (zhangxing090731@163.com).
[1] PLA Unite of 93995, Xi'an 464100, China. [2] Hunan First Normal University, Changsha 410073, China. [3] ATR Key Laboratory, National University of Defense Technology, Changsha 410073, China.

base approximation into a lower dimensional model. The second improved approach splits the entire 3D imaging model into several lower-dimensional sparse representation models, resulting in superior dimension reduction. These time-domain methods are tractable in terms of memory and computational requirements, and do not require ad-hoc solving algorithms. The 3-D image is generated through solving the time-domain representation sparse model by l_1-regularized [26, 27]. Experimental results on two targets demonstrate the effectiveness and efficiency of the proposed time-domain approach.

2. MULTI-VIEW COLLATED SAR DATA

In the present work, a single polarization is studied, and multi-view SAR data is interpreted in terms of a 3-D spatial spectrum obtained by a 3D Fourier transform of the target reflectivity function for a particular view's angles (ϕ, θ) defined by the expression

$$G(w_x, w_y, w_z) = \sum_{n=1}^{N} g(x, y, z; \phi, \theta) \cdot e^{-j(x_n w_x + y_n w_y + z_n w_z)} \tag{1}$$

Here, $g(x, y, z; \phi, \theta)$ is the reflectivity function, and $G(w_x, w_y, w_z)$ is the spatial spectrum. For narrow angles, it is reasonable to assume that the reflectivity of the scattering center is isotropic. We subdivide the wide-field survey into a set of possible sub-apertures and assume that the scattering is locally isotropic at each sub-aperture. Once we have obtained sub-aperture images, an overall wide-angle image can be formed by fusing the narrow-aperture images in an appropriate manner. Supposing that $I(x, y, z)$ is the 3-D image in the narrow-aperture with center angle (ϕ, θ), the signal model can be rewritten as

$$G(w_x, w_y, w_z) = \sum_{n=1}^{N} I(x, y, z) \cdot e^{-j(x_n w_x + y_n w_y + z_n w_z)} \tag{2}$$

Figure 1 depicts a typical collection geometry for multi-view data. $\tilde{\mathbf{D}}_k = [G(w_x^{(i,j,k)}, w_y^{(i,j,k)}, w_z^{(i,j,k)})]_{i=1,j=1}^{Mf_k, Nf_k}$ are the samplings in aspect k, and $k = 1, \cdots, K$. Mf_k is the number of samples in frequency, and Nf_k is the number of samples in azimuth.

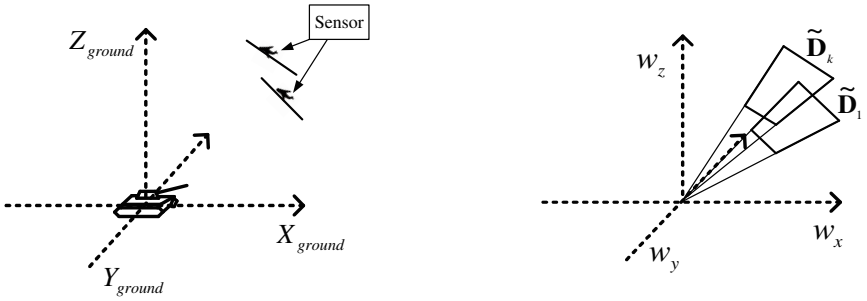

(a) Collection geometry (b) Fractions in wavenumber coordinate system

Figure 1. Multiple-aspect SAR collection geometry.

The 3-D coordinates of each sampling in the wavenumber domain are $w_x^{(i,j,k)} = -4\pi f_i \cos\theta_{j,k} \cos\phi_{j,k}/c$, $w_y^{(i,j,k)} = -4\pi f_i \cos\theta_{j,k} \sin\phi_{j,k}/c$, $w_z^{(i,j,k)} = -4\pi f_i \sin\theta_{j,k}/c$. Here, c is the speed of light. By the projection-slice theorem, each aperture is a fraction of the wavenumber domain $G(w_x, w_y, w_z)$. For convenience, the multi-view SAR dataset is denoted as $\{\tilde{\mathbf{D}}_k\}_{k=1}^{K}$, and all measurements are reshaped into a vector $\tilde{\mathbf{d}} = [d_m]_{m=1}^{M}$. Their coordinates can also be placed into a vector $\mathcal{H}_{\mathcal{M}} = \{\hbar_m\}_{m=1}^{M}$. $\hbar_m = (w_{x,m}, w_{y,m}, w_{z,m})$ is the m-coordinate, while d_m is the corresponding measurement.

3. TIME-DOMAIN SPARSE REPRESENTATION FOR 3-D IMAGING

Sparse representation-based 3D imaging methods define a set of locations in the 3D imaging space as voxels.

$$\mathcal{Q}_{\mathcal{M}} = \{\lambda_1, \ldots, \lambda_N\} = \{(x_n, y_n, z_n)\}_{n=1}^{N} \tag{3}$$

N is the number of voxels. In most existing approaches, the locations are chosen on a uniform rectilinear grid, and the dictionary is constructed in the frequency domain.

$$\tilde{\mathbf{\Psi}} = F(\mathcal{H}_{\mathcal{M}}, \mathcal{Q}_{\mathcal{M}}) = \left[e^{-j(x_n w_{x,m} + y_n w_{y,m} + z_n w_{z,m})}\right]_{m,n} \tag{4}$$

Here, m indexes the sampling of measurements in the down row of the wavenumber domain, and n indexes the locations across columns. Then, the measured data can be approximated as,

$$Q_{\mathrm{FD}}(\mathcal{Q}_{\mathcal{M}}): \quad \tilde{\mathbf{d}} = \tilde{\mathbf{\Psi}} \cdot \mathbf{s} + \tilde{\mathbf{v}} \tag{5}$$

Here, $\tilde{\mathbf{d}}$ is the M-dimensional measurement vector of the multi-view SAR data; $\tilde{\mathbf{v}}$ is the noise vector; and $\mathbf{s}$ is the N-dimensional scattering amplitude vector to be reconstructed.

$$\hat{\mathbf{s}} = \arg\min \|\mathbf{s}\|_0 \ \text{ s.t. } \ \left\|\tilde{\mathbf{\Psi}} \cdot \mathbf{s} - \tilde{\mathbf{d}}\right\|_2 < \varepsilon \tag{6}$$

$\hat{\mathbf{s}}$ is the solution of the sparse optimization problem (6), which has a complex amplitude value in row n, if a scattering center is located at $\lambda_n = (x_n, y_n, z_n)$ and is otherwise zero in row n.

In this paper, we develop a sparse representation model in the time domain. On the k-th aspect, the 2-D frequency domain response of a scattering center at $\lambda_n = [x_n, y_n, z_n]^T$ is,

$$\tilde{E}(\mathcal{H}_{\mathcal{M},k}|\lambda_n) = \left[\exp[-j(x_n w_{x,k}^{(i,j)} + y_n w_{y,k}^{(i,j)} + z_n w_{z,k}^{(i,j)})]\right]_{i=1,j=1}^{Mf_k, Nf_k} \tag{7}$$

The response is an $Mf_k \times Nf_k$ matrix, denoted as $\tilde{\mathbf{E}}_{k,n} = \tilde{E}(\mathcal{H}_{\mathcal{M},k}|\lambda_n)$. Then $\tilde{\mathbf{E}}_n$ is transformed to the time domain.

$$\mathbf{E}_{k,n} = \mathcal{F}_2^{-1} \cdot B \cdot \tilde{\mathbf{E}}_{k,n} \tag{8}$$

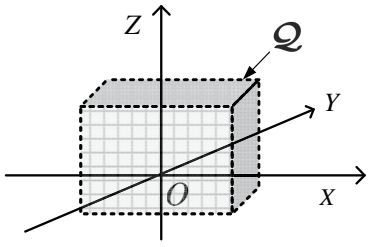

(a) The original imaging region

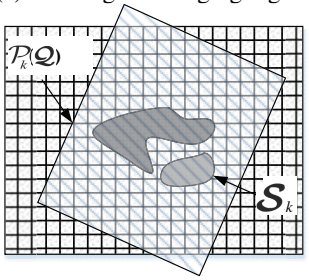

(b) 2-D projection of original imaging region and target support zone

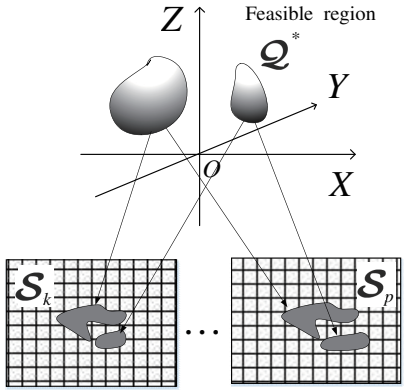

(c) Feasible region for 3-D imaging

Figure 2. Sketch of the original imaging region, its 2-D projection, target support zone and 3-D feasible region.

Here, $\mathcal{F}_2^{-1}(\cdot)$ represents the 2-D inverse fast Fourier transform, and $B(\cdot)$ represents resampling 2-D response $\tilde{E}(f,\phi)$ in polar coordinates into a uniform grid in Cartesian coordinates. Mz_k and Nz_k are the numbers of points in row and column. In this paper, they are set as $Mz_k = Mf_k$ and $Nz_k = Nf_k$. Then $\mathbf{E}_{k,n}$ is stacked into an $Mz_k \cdot Nz_k$-dimensional vector. It is the signal component of the k-aspect of scattering center at position λ_n. The original time-domain dictionary is given by

$$\mathbf{\Psi} = [\ \mathbf{\Phi}_1 \quad \cdots \quad \mathbf{\Phi}_N\ ] = \begin{bmatrix} \varphi_{1,1} & \cdots & \varphi_{1,N} \\ \vdots & \ddots & \vdots \\ \varphi_{K,1} & \cdots & \varphi_{K,N} \end{bmatrix} \tag{9}$$

Here, $\mathbf{\Phi}_n$ is the n-th column of the dictionary. It consists of all the time domain signal components of λ_n.

Finally, $\tilde{\mathbf{D}}_k$ is transformed to the time domain by $\mathbf{D}_k = \mathcal{F}_2^{-1} \cdot B \cdot \tilde{\mathbf{D}}_k$, and reshape $\mathbf{D}_k$ into a measurement vector $\mathbf{d}_k = [d_m]_{m=1}^{M_k}$, $M_k = Mz_k \cdot Nz_k$. The measured data can be approximated as,

$$Q_{\mathrm{TD}}(\mathcal{Q}_{\mathcal{M}}): \quad \mathbf{d} = \mathbf{\Psi} \cdot \mathbf{s} + \mathbf{v}, \text{ here } \mathbf{d} = \begin{bmatrix} \mathbf{d}_1 \\ \vdots \\ \mathbf{d}_{N_{ap}} \end{bmatrix} \tag{10}$$

Here, $\mathbf{v}$ is a time-domain noise vector. s is the N-dimensional scattering amplitude vector to be reconstructed.

An l_1-regulated sparse optimization problem [26, 27] is solved to obtain $\hat{\mathbf{s}}^*$,

$$\hat{\mathbf{s}}^* = \arg\min \left\{ \|\mathbf{\Psi} \cdot \mathbf{s} - \mathbf{d}\|_2^2 + \lambda \|\mathbf{s}\|_1 \right\} \tag{11}$$

According to the time-frequency duality principle, the frequency-domain model and time-domain model are equivalent. $\hat{\mathbf{s}}^*$ has amplitude values in the row if a scattering center is located at $\lambda_n = (x_n, y_n, z_n)$ and is zero otherwise. $\hat{\mathbf{s}}^*$ maps to the 3-D image, by the relation $I(x_n, y_n, z_n) = \hat{\mathbf{s}}^*(n)$.

4. BASIC TIME-DOMAIN APPROACH TO 3-D IMAGING

In this section, a basic method based on the time-domain spars representation (10) is proposed. Its specific procedure for constructing a time-domain dictionary, such that the dictionary is a sparse matrix, is presented. An approach to identify feasible regions is performed by selecting a set of locations in the 3-D space where the image reconstruction will take place.

4.1. Time-Domain Sparse Dictionary

Figure 3 shows an example of $\tilde{\mathbf{E}}_{k,n}$ and $\mathbf{E}_{k,n}$. It can be seen that the energy of the time-domain response is concentrated in a narrow region. The amplitude in the large region is well below the peak. It does not depend on the measurement data but is a natural feature of the scattering center model. Time-domain

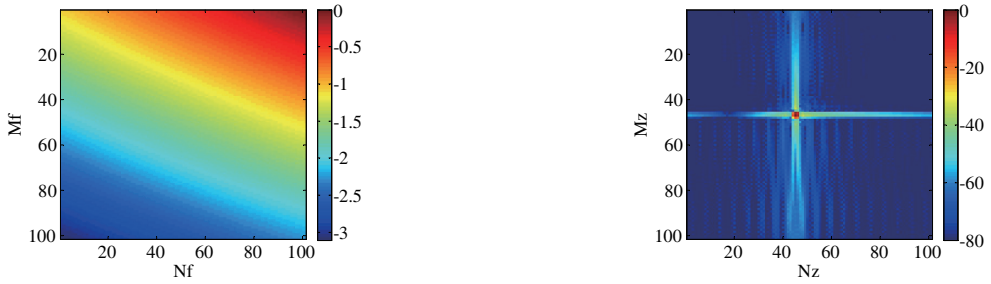

(a) Frequency domain (b) Time domain

Figure 3. One-aspect responses of a 3D scattering center.

methods truncate the finite-amplitude region such that the response is a sparse matrix. Since $\boldsymbol{\varphi}_{k,n}^{o}$ is the signal component of $\bar{\lambda}_n$ in the k-th aspect, let

$$\boldsymbol{\varphi}_{k,n}^{o}: \quad \boldsymbol{\varphi}_{k,n}^{o}(i) = \begin{cases} 0 & |\boldsymbol{\varphi}_{k,n}(i)| < \xi_n \\ \boldsymbol{\varphi}_{k,n}(i) & else \end{cases}, \quad i = 1, \cdots, Nz_k \cdot Mz_k \tag{12}$$

Here ξ_n is an adaptive threshold. Its value is determined by a function, $\xi_n = \max_{i=1}^{Nz_k \cdot Mz_k}(|\boldsymbol{\varphi}_{k,n}(i)|) \cdot 10^{\beta_d/20}$. $\beta_d < 0$ is an empirical threshold for the entire dictionary. After all $\boldsymbol{\varphi}_{k,n}$ have been processed, the time-domain dictionary becomes a spare matrix by replacing $\boldsymbol{\varphi}_{k,n}$ with $\boldsymbol{\varphi}_{k,n}^{o}$. We still label the present dictionary as $\boldsymbol{\Psi}$ and let $\boldsymbol{\varphi}_{k,n}^{o} \to \boldsymbol{\varphi}_{k,n}$.

When $\beta_d > -\infty$, $\boldsymbol{\Psi}$ is a sparse matrix. Let N_o be the number of non-zero elements and $\eta = N_o/(M \cdot N)$ the fraction of non-zero elements. Denote the degree of sparsity of the lexicographic matrix by η. The larger the β_d is, the smaller the η is, and the sparser $\boldsymbol{\Psi}$ is beneficial for reducing the data size of the dictionary.

4.2. Shrinking of 3-D Imaging Region

We use the target information provided by the 2D images to reduce the feasible area for 3D imaging. Suppose that $\mathcal{Q}$ is the 3-D imaging space, $\mathcal{P}_k(\mathcal{Q})$ the projected region of $\mathcal{Q}$ on the k-th 2-D image, and $\mathcal{S}_k$ the target area detected from the k 2-D image. $\mathcal{S}_k$ is referred to as the 2-D support zone of the target. It indicates the potential region where the scattering center of the target may lie. Figures 2(a) and 2(b) show sketches of $\mathcal{Q}$, $\mathcal{Q}_k(\mathcal{Q})$, and $\mathcal{S}_k$. Commonly, the 3-D imaging space is set as a rectangular parallelepiped. $\mathcal{P}_k(\mathcal{Q})$ is always larger than the 2-D range of the target, as far as the scattering centers of most artificial targets are sparse on a 2-D image. Thus, $\mathcal{P}_k(\mathcal{Q})$ is larger than $\mathcal{S}_k$.

When the flight passes parallel to ground (XOY plane), the projection transformation between 3-D locations and 2-D locations at the k aspect is given by,

$$\begin{bmatrix} x' \\ y' \end{bmatrix}_k = \mathbf{H}_k \cdot \begin{bmatrix} x \\ y \\ z \end{bmatrix}, \quad \text{here} \quad \mathbf{H}_k = \begin{bmatrix} -\sin\phi_k & \cos\phi_k & 0 \\ -\cos\theta_k\cos\phi_k & -\cos\theta_k\sin\phi_k & -\sin\theta_k \end{bmatrix} \tag{13}$$

If the flight path is not parallel to the XOY plane, our approach is the same except that $\mathbf{H}_k$ needs a modification. The projection transformation can be derived from signal-processing theory [28] or photogrammetry theory [29, 30]. Without loss of generality, the flight path is assumed to be parallel to the XOY plane in the following.

With $\mathcal{S}_k$ and transformation (13), the parts of A that no scattering center located at can be quickly discarded. $\bar{\lambda} = [x, y, z]^T$ is assumed to be an arbitrary location in the 3D imaging range, $\bar{\lambda} \in \mathcal{Q}$. And $\mathcal{P}_k(\bar{\lambda}) = \mathbf{H}_k \cdot \bar{\lambda}$ is its projection location on the k-th 2-D image. If $\mathcal{Q}_k(\bar{\lambda})$ is in $\mathcal{S}_k$, such a case is referred to as "$\bar{\lambda}$ associated with $\mathcal{S}_k$", denoted as $\mathcal{P}_k(\bar{\lambda}) \in \mathcal{S}_k$. $\bar{\lambda}$ is considered as a candidate site for 3D imaging only if it is associated with more than two $\mathcal{S}_k$. Otherwise, it is an invalid site. The 3D-imaging feasible region consists of all candidate sites.

Support zones are detected from images by target detection methods such as constant false alarm rate detection or image segmentation methods. The principle of determining the support region is to maintain that the scattering centers of all regions may be located at. In this paper, we use a hard-threshold image segmentation method to generate the support region of the target on each 2-D SAR image. It may be stated as follows,

$$\mathcal{S}_k : \{x, y | \left|I_k'(x, y)\right| > \max(\left|I_k'(x, y)\right|) \cdot 10^{\beta_s/20}$$

Here β_s is a threshold set manually in this paper. It is reasonable to set a lower threshold to ensure that all potential target regions are included. While this may introduce non-target regions, it does not cause trouble as the subsequent correlation mechanism can overcome it. A logical function $\ell_k'(\bar{\lambda})$ is defined to indicate whether $\bar{\lambda}$ is assigned to $\mathcal{S}_k$.

$$\ell_k'(\bar{\lambda}) = \begin{cases} 1 & \mathcal{P}_k(\bar{\lambda}) \in \mathcal{S}_k \\ 0 & \mathcal{P}_k(\bar{\lambda}) \notin \mathcal{S}_k \end{cases} \quad k = 1, \ldots, K \tag{14}$$

The 3-D imaging feasible region is defined as: for any arbitrary location in feasible region, Formula (15) is satisfied.

$$\ell(\bar{\lambda}) = \sum_{k=1}^{K} \ell'_k(\bar{\lambda}) \geq \beta_\ell \tag{15}$$

Here, the feasible region, denoted as $\mathcal{Q}^*$, is a part of $\mathcal{Q}$; $\bar{\lambda}$ is an arbitrary location in the feasible region; $\beta_\ell (2 \leq \beta_\ell \leq K)$ is a priori threshold. The mechanism of the feasible region generation is sketched in Figure 2(c). Since the feasible region has been found, it is advisable to construct a dictionary for only the feasible region rather than $\mathcal{Q}$, which will reduce the columns of the separable dictionary.

By definition, the feasible region is continuous. People should find it and then sample it into a set of candidate locations $\mathcal{Q}^*_{\mathcal{M}}$. In practice, it can be generated in a simple way. The first is to choose a set of locations on a uniform rectilinear grid $\mathcal{Q}_{\mathcal{M}} = \{\bar{\lambda}_n\}_{n=1}^{N}$. Secondly, it projects all N locations onto K 2-D images, then computes the value of the logical function $\ell'_k(\bar{\lambda}_n)$ and the support function $\ell(\bar{\lambda}_n)$. According to $\ell(\bar{\lambda}_n)$, a large number of 3-D locations are eliminated, while the remaining locations are the feasible region.

$$\mathcal{Q}^*_{\mathcal{M}}: \quad \ell(\bar{\lambda}_n) = \sum_{k=1}^{K} \ell'_k(\bar{\lambda}_n) \geq \beta_\ell, \quad n = 1, \cdots N \tag{16}$$

5. TWO EXTENSION TIME-DOMAIN APPROACHES TO 3-D IMAGING

In this section, two improved methods are extended by taking some preprocessing of the measured data. The first exploits the fact that the target region is considerably smaller than the extent of the 2-D image. The second one exploits the fact that the target region consists of several separable subareas.

5.1. The First Extension Method

The energy of the 2D time-domain response of each artificial target is concentrated in a few finite regions, while the energy of the SAR data is well distributed in the frequency domain. An example is shown in Figure 4. If the measurement data of target are noiseless, or a target-separation procedure has been performed to them [31, 32], resulting in significant regions of low energy in the 2-D image.

(a) Frequency domain (b) Time domain

Figure 4. SAR data of a target at one aspect.

By setting the low energy region to zero, the residual region that remains nonzero is taken to be the support region of the target signal, denoted as $\mathcal{R}_k$. It can be generated by either a target separation method or an image segmentation method. The implications of $\mathcal{R}_k$ and target region $\mathcal{S}_k$ are quite different, although they can be obtained by the same method with different thresholds. While the principle for determining $\mathcal{S}_k$ is to include all regions where the scattering center is likely to be located, the principle for determining $\mathcal{R}_k$ is to maintain a sufficient signal component for the target.

After truncation, the measurement vector $\mathbf{d}$ is constructed using the truncated time-domain measurement data, and the rows with zero measurements in the sparse representation model are merged.

The zero elements in $\mathbf{d}$ are indexed by m_q, where $q = 1, \ldots, M_o$, and M_o is the number of zero elements. The corresponding rows of $\mathbf{\Psi}$ are subsequently consolidated as follows.

$$\mathbf{d}^* = \begin{bmatrix} \mathbf{d}' \\ 0 \end{bmatrix}, \quad \mathbf{\Psi}^* = \begin{bmatrix} \mathbf{\Psi}' \\ \psi \end{bmatrix}$$

Here, $\mathbf{d}'$ is the remainder by removing the zero-value elements in $\mathbf{d}$, $M' = M - M_o$. The sub-dictionary $\mathbf{\Psi}'$ is the remainder of $\mathbf{\Psi}$ by removing the corresponding rows. $1 \times N$ merged row vector $\psi = [\Delta\varphi_1, \ldots, \Delta\varphi_N]$ is computed by,

$$\psi(n) = \sum_{q=1}^{Q} \mathbf{\Psi}(m_q, n), \quad \text{and} \quad \Delta\varphi_n = \sum_{q}^{Q} \left|\varphi_{m_q,n}\right| \tag{17}$$

The measurement corresponding to this row is set to zero. After such a dimension reduction, $\mathbf{d}^*$ is an $M^* \times 1$ vector, and $\mathbf{\Psi}^*$ is an $M^* \times N$ matrix, $M^* = M' + 1$. The sparse representation model of the basic approach is reduced to a lower dimensional one.

$$Q_{\mathrm{TD}}^*(\mathcal{Q}_{\mathcal{M}}^*): \quad \mathbf{d}^* = \mathbf{\Psi}^* \cdot \mathbf{s} + \mathbf{v} \tag{18}$$

We can generate the sparse vector $\hat{\mathbf{s}}^*$ by solving an optimization as expression (11) and interpolates s into a 3-D image by the same way as the basic method.

5.2. The Second Extension Method

In some cases, the target area $\mathcal{R}_k$ consists of numerous tiny areas or can be segmented into several smaller regions by SAR image-segmentation technology [33, 34]. Let R_k be the number of subareas in the k-th 2-D image and denote the subareas as $\mathcal{R}_{r,k}^*$, $r = 1, \cdots, R_k$. If there is a sub-feasible region of $\mathcal{Q}_{\mathcal{M}}^*$ unconnected with the rest, and the following conditions,

- **Condition 1:** All candidate locations in this sub-feasible region are assigned to a sub-queue $\{\mathcal{R}_{r_p,k_p}^*\}_{p=1}^P$.
- **Condition 2:** no candidate site outside this sub-feasible region is associated with $\{\mathcal{R}_{r_p,k_p}^*\}_{p=1}^P$.

are satisfied, the sub-feasible regions are defined as independent sub-feasible regions. Suppose that there are Q ($Q \geq 1$) independent sub-feasible regions in a 3-D imaging task. When $Q = 1$, the whole $\mathcal{Q}^*$ is tokenized as an independent sub-feasible region. Since the 3-D imaging aperture is not wide, and the baselines of the 2-D SAR images are not far from each other, it is common for an artificial target to have more than one independent sub-feasible region. They are indexed by q and denoted as $\mathcal{Q}_{\mathcal{M},q}^{**}$. The corresponding sub-queue is denoted as $\mathcal{R}_q^{**} = \{\mathcal{R}_{r_p,k_p}^*\}_{p=1}^P$.

The independent sub-feasible regions are identified as follows. First, the entire feasible region is separated into several sub-feasible regions using the connected component labeling method. Second, the extraction of independent sub-feasible regions can be done by an index-labeling step. Let a $Q \times R_k$ matrix $\mathbf{l}_k = [l_{q,r}^k]_{q,r}$ label whether these locations in the separated feasible region associated to $\mathcal{R}_{r,k}^*$ on the k-th 2-D image. If the q-th 3D subregion is associated with $\mathcal{R}_{r,k}^*$, $l_{r,q}^k = 1$. Figure 5 is a schematic

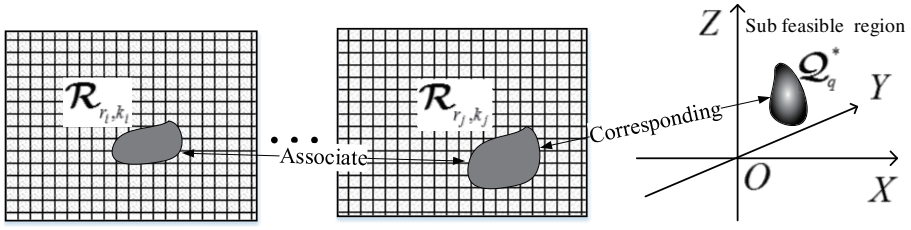

Figure 5. Diagrammatic sketch of an independent sub-feasible region.

of a 3-D independent feasible region and a 2-D target subarea, and the correlation between them. A matrix $\mathbf{L} = [\mathbf{l}_k]$ labels all the correspondences. Perform a matrix elementary operation to transform $\mathbf{L}$ into a block matrix. Each block initializes an independent sub-feasible region, which may consist of more than one disconnected subregion.

$$\mathbf{L}_B = \begin{bmatrix} \mathbf{b}_1 & \cdots & \mathbf{0} \\ \vdots & \ddots & \vdots \\ \mathbf{0} & \cdots & \mathbf{b}_{Q_S} \end{bmatrix}$$

Then, we divide the entire feasible region into Q independent subregions, $\mathcal{Q}^{**}_{\mathcal{M},q}$, $q = 1, \cdots, Q$. The time-domain measurement vector of the separable region $\mathcal{R}^{**}_q$ is denoted as $\mathbf{d}_q = [\mathbf{d}_{r_p,k_p}]^P_{p=1}$. As a few elements of that vector are nonzero, every subregion utilizes the sparse-representation model (17) for imaging, similar to the first improved method.

$$Q^*_{\mathrm{TD}}(\mathcal{Q}^{**}_{\mathcal{M},q}): \quad \mathbf{d}^{**}_q = \mathbf{\Psi}^{**}_q \cdot \mathbf{s}^{**}_q + \mathbf{v} \tag{19}$$

where $\mathbf{d}^{**}_q$ is a condensed $\mathbf{d}_q$, and M^{**}_q is its length. The dictionary $\mathbf{\Psi}^{**}_q$ is an $M^{**}_q \times N^{**}_q$ matrix. N^{**}_q is the number of candidate locations of $\mathcal{Q}^{**}_{\mathcal{M},q}$.

If $Q \geq 2$, the sparse-representation model of 3-D imaging for the whole region, which is high-dimensional, is divided into a set of low-dimensional models.

$$Q^{**}_{\mathrm{TD}}(\mathcal{Q}^*): \quad \begin{cases} \mathbf{d}^{**}_1 = \mathbf{\Psi}^{**}_1 \cdot \mathbf{s}^{**}_1 + \mathbf{v} \\ \vdots \\ \mathbf{d}^{**}_Q = \mathbf{\Psi}^{**}_Q \cdot \mathbf{s}^{**}_Q + \mathbf{v} \end{cases} \tag{20}$$

After solving every sub-model $\mathbf{d}^{**}_q = \mathbf{\Psi}^{**}_q \cdot \mathbf{s}^{**}_q + \mathbf{v}$ in (20) respectively and mapping every $\mathbf{s}^{**}_q$ to a sub-3-D image, the whole 3-D image is a superimposition of all sub-images. As $Q > 2$, $Q \geq 2$, $M^{**}_q < M$, $N^{**}_q < N$, and $M^{**}_q \times N^{**}_q << M \times N$, the dimension of $\mathbf{\Psi}^{**}_q$ is much lower than $\mathbf{\Psi}$ and $\mathbf{\Psi}^*$, let alone $\tilde{\mathbf{\Psi}}$. Since the large-scale problem has been transformed into a minor-scale problem of size Q, the imaging efficiency will be considerably improved over the basic and first improved approaches.

Essentially, condition 1 is a bit too unscrupulous for most applications. Due to the approximate orthogonality of signals of the separated regions [32], only if $\mathcal{Q}^{**}_{\mathcal{M},q}$ is unconnected from the others, and all locations in $\mathcal{Q}^{**}_{\mathcal{M},q}$ are associated with a sub-queue $\mathcal{R}^{**}_q = \{\mathcal{R}^*_{r_p,k_p}\}^P_{p=1}$, it is practical to use model (20) for 3-D imaging in numerous applications.

6. EXPERIMENTAL RESULTS

This section presents results of the application of the three time-domain methods to synthetic SAR data of a simulated target and data of an SLICY-like target generated by electromagnetic magnetism (EM) code. For comparison, we also reconstruct 3-D images using the frequency domain method. The experiments use the large-scale l_1-regularized least squares method [27] and the corresponding *l1_ls* MATLAB solver toolbox [35] to solve the optimization problems (6) and (11) of sparse representation.

6.1. Experiment of Simulated Target

This experiment details the performance of our time-domain approach on a simulated target. The target consists of 11 scattering centers located in the range $\mathcal{Q} = \{x, y, z | -2 \leq x < 2, -2 \leq y < 2, 0 \leq z < 1\}$ meters. The coordinates are listed in Table 1. We simulate SAR data of five aspects by GTD model [36]

$$G(w_x, w_y, w_z) = \sum_{i=1}^{P} A_i \cdot (jf/f_c)^{\alpha_i} \cdot e^{-j(x_i w_x + y_i w_y + z_i w_z)} \tag{21}$$

Here A_i is generated randomly in the range $[-16,\ 0]$ dB of the maximum. α is set to one of $[-1, -0.5, 0, 0.5, 1]$, randomly. SAR data are simulated at five aspects (θ_k, ϕ_k), $\phi_k = 5°$, $k = 1, \ldots, 5$, and $\theta_1 = 22.5°$, $\theta_2 = 23.5°$, $\theta_3 = 24.5°$, $\theta_4 = 25.5°$, $\theta_5 = 27.5°$. The aperture is $\widehat{\phi} = 5°$ and the

Table 1. Locations of the 11 scattering centers of target.

Index	$[x, y, z]$	Index	$[x, y, z]$
1	$[-1.727, 0.890, 0.771]$	**7**	$[1.598, -0.499, 0.512]$
2	[0.975,0.750,0.635]	**8**	$[-1.727, 0.250, 0.771]$
3	[0.975,0.499,0.635]	**9**	[1.598,0.8895,0.512]
4	$[0.975, -0.499, 0.635]$	**10**	$[-1.727, -0.250, 0.771]$
5	$[-1.727, -0.890, 0.771]$	**11**	[0.499,0.044,0.685]
6	[1.598,0.499,0.512]		

spacing $\Delta\phi = 0.1°$. The frequency band is 8.5 to 9.5 GHz with a frequency step of $\Delta f = 30$ MHz. We add zero-mean white Gaussian noise with a signal-to-noise of -20 dB. In this paper, we define the signal-to-noise ratio (SNR) as the ratio of the peak image amplitude to the noise standard deviation in the 2D image domain. It is expressed in the dB scale as $SNR = 20 * \log_{10}(|pk_{image}|/\sigma_{img})$. The five SAR images with noise are shown in Figure 6(a).

The 3D imaging space $\mathcal{Q}$ is first meshed into a set of 3D locations with spacings $\Delta x = 0.1$ m, $\Delta y = 0.1$ m, $\Delta z = 0.1$ m, resulting in a total of $N = 18491$ locations. The traditional methods

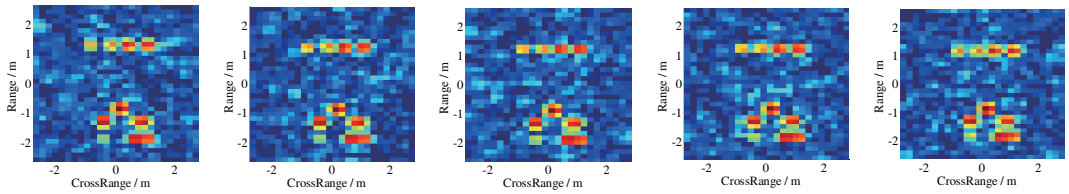

(a) Five aspects of SAR data in image domain, the dynamic amplitude range for display is [–40,0] dB

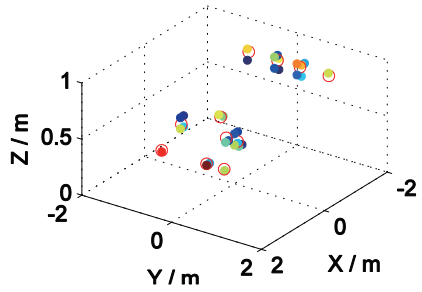

(b) 3-D image generated by frequency-domain method

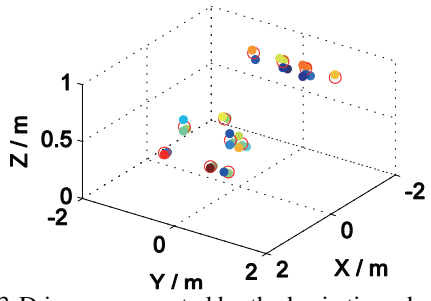

(c) 3-D image generated by the basic time-domain method

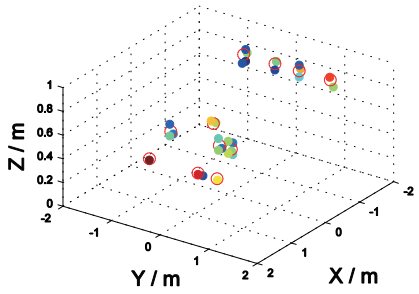

(d) Image generated by the first improved method

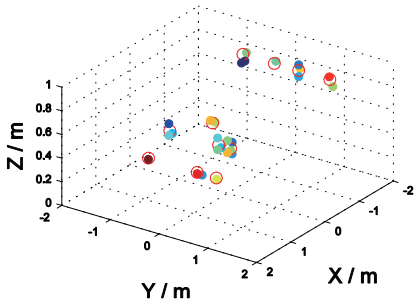

(e) Image generated by the second improved method

Figure 6. 3-D imaging results of time-domain method and frequency method of simulated target.

have to construct a dictionary for all the locations, in which the dimensions of dictionary are $M \times N = 4420 \times 18491$. In the basic time-domain approach, the threshold is set to $\beta_s = -30\,\mathrm{dB}$, $\beta_\ell = 5$ to generate the feasible region $\mathcal{Q}^*_{\mathcal{M}}$. As a result, there are only $N^* = 2520$ locations remaining in the feasible region. It is only $N^*/N = 13.6\%$ of the original. The threshold $\beta_d = -50\,\mathrm{dB}$ is used to construct the time-domain dictionary. The dimensions of the dictionary are $M \times N^* = 4420 \times 2520$, while the proportion of nonzero elements is $\eta = 7.1\%$. It is claimed that the data size of the dictionary of our basic method is only $13.6\% \times 7.1\% = 0.97\%$ of the traditional frequency-domain dictionary. In addition, it has been found that identifying feasible 3D imaging regions helps to overcome noise and speckles. The energy of the target region on the 2-D image is constantly elevated, while high-energy noise or speckles arise randomly. There is a slight probability that the speckles will appear at all β_ℓ 2-D locations. As a result, some of the speckles that might have appeared were discarded. These dominance properties are not related to the solution algorithm but are a property of the time-domain approach.

The sparse representation model is then solved with the sparsity parameter $\lambda = 7$ for the basic time domain method and $\lambda = 1000$ for the frequency domain method to generate 3-D images. Sparse parameters were manually selected by visual inspection of the images. Automatic selection of sparse parameter is an ongoing area of research [37, 38].

Figure 6(b) is the image reconstructed by the frequency-domain sparse-representation method. Figure 6(c) is the image reconstructed by the basic time-domain method. The top 25 dB magnitude voxels are displayed (the same below except specifically marked). The two 3D images are almost identical. The features in these sparsely reconstructed images are adequately resolved. The remaining 3D voxels are located in a neighborhood of the true scattering center. This is reasonable since we deliberately set their positions not to be exactly inside the grid points. The motivation for this is to check the robustness of the proposed method.

The basic time-domain method takes 9.6 seconds to obtain the solution, while the frequency-domain method takes 843.4 seconds. In detail, the time-domain method needs 35 iterations and 11.7 preconditioned conjugate gradient (PCG) iterations for each iteration, on average. The frequency domain method requires 72 iterations and 34.5 PCG iterations on average. The time-domain approach is more efficient. Better temporal efficiency may benefit from the lower dimension of the sparse representation problem, as well as the smaller data size of the dictionary. Moreover, a time-domain dictionary consisting of cut-off responses may be helpful to avoid noise jamming and accelerate convergence.

Also, the experimental results of the two modified methods are presented. For the first improved method, the target separation is implemented in this experiment by a hard thresholding method. The empirical threshold for separation is $-25\,\mathrm{dB}$ of the image peak, which is chosen based on the noise level. Regions above and equal to $-25\,\mathrm{dB}$ are assigned to the target region, while regions below $-25\,\mathrm{dB}$ are assigned to the noise region. Since the SAR image has a 20 dB signal-to-noise ratio, some noise regions may remain. Since the residual noises on different images are uncorrelated, they are dislodged by the imaging method. As shown in the following experiments, the residual noise barely contributes to the 3-D imaging. Furthermore, for the second improved method, the image segmentation is implemented by a watershed method as used in [34]. We then solve the sparse representation model for the two modified methods with the same sparsity parameter $\lambda = 7$.

Imaging results are shown in Figures 6(d) and 6(e), as Figure 6(d) is reconstructed by the first improved method, and Figure 6(e) is the result of the second improved method. Locations of the remaining voxels are approximately the same as Figure 6(b), apart from some slight difference in amplitudes. It indicates that both extended methods are effective for formalizing 3D images from multi-view data. Both methods show significant efficiency gains over traditional methods and our base method. In the first improved method, the dimensions of the dictionary are $M^* \times N^* = 418 \times 2520$, considerably lower than dimensions of the traditional $M \times N = 4420 \times 18491$, also lower than the dimensions of the basic time-domain one $M^* \times N^* = 4420 \times 2520$. Obviously, this is only 1.29% and 9.45% of the frequency domain dictionaries, respectively. The computation time of the solution is 2.6 seconds. In the second improved method, the imaging task is broken down into two lower dimension sparse-representation problems: one is $M^{**} \times N^{**} = 165 \times 1032$ dimensional; the other is $M^{**} \times N^{**} = 223 \times 1418$ dimensional. The computation times of the solutions are 0.97 and 1.21 seconds, respectively.

6.2. Experiment of EM Code Data of SLICY Target

This section presents the results of applying our algorithm to the SLICY target synthetic data. The data were generated by an EM code capable of accurately simulating arbitrary EM scattering measurements obtained by irradiating a faceted model target. We set the parameters for the synthetic data as: central frequency $f_c = 10\,\text{GHz}$, bandwidth $BW = 4\,\text{GHz}$, frequency step $\Delta f = 30\,\text{MHz}$.

We then produce measurements on the scale of 1/5 of a SLICY target, at three periastron angles. The center azimuth and elevation are $\phi_{c,1} = -85.7°$, $\phi_{c,2} = -86.7°$, $\phi_{c,3} = -87.7°$, $\theta_1 = 30°$, $\theta_2 = 33°$, $\theta_3 = 35°$. All apertures are $\widehat{\phi} = 5°$, and the azimuthal sample spacing is $\Delta\phi = 0.2°$. We add white Gaussian noise with SNR $= 30\,\text{dB}$ in the 2-D image domain. Figures 8(a) and 8(b) show the SLICY target and three simulated SAR images, in which the dynamic amplitude range for display is $[-35, 0]\,\text{dB}$.

We set the original 3-D imaging range as $\{x, y, z | -3m \le x < 3m, -3m \le y < 3m, -1m \le z < 3m\}$, which corresponds to the target size. We then meshed it into a grid with spacings $\Delta x = 0.05\,\text{m}$, $\Delta y = 0.05\,\text{m}$, $\Delta z = 0.05\,\text{m}$, resulting in $N = 120 \times 120 \times 80 = 1152000$ locations. If a traditional method were employed, the dimensions of the dictionary would be $M \times N = 10530 \times 1152000 \approx 1 \times 10^{10}$. Dealing with a problem of such enormous dimension is as difficult as it is extraordinarily difficult, both with respect to the larger amount of data and with respect to the computation. For instance, it would be necessary to store the dictionary matrix in a 1×10^{10} dimensional complex space. If the dictionary were stored with double precision, the dictionary's data size would be $M \times N \times 2 \times 8$ bytes, which is more than 160 GB! Performing such a huge dimension problem in a common experimental environment is a difficult task.

Figures 7(c)∼7(h) show the imaging results of the time-domain methods with parameters $\beta_s =$

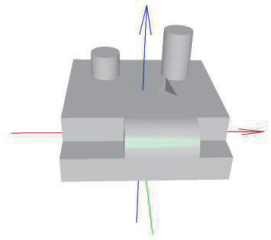

(a)1/5 scaled SLICY target

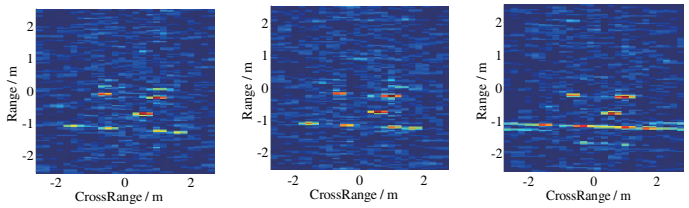

(b) Three SAR images

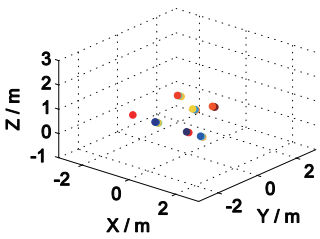

(c) Imaging result of basic method

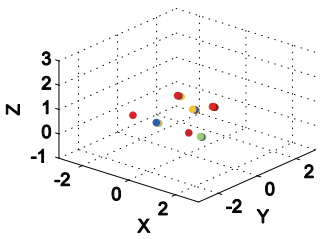

(d) Imaging result of first improved method

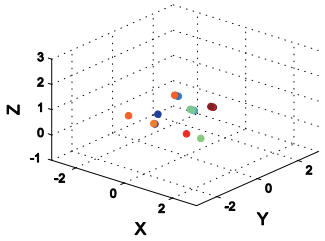

(e) Imaging result of second improved method

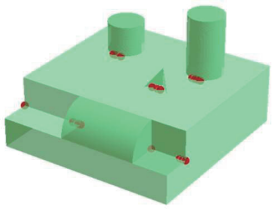

(f) The superposition of basic method

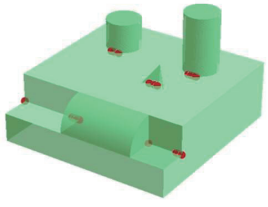

(g) The superposition of first improved method

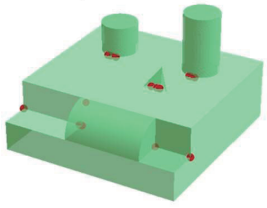

(h) The superposition of second improved method

Figure 7. 3-D imaging results of three time-domain methods at azimuth $\phi = 86.7°$.

$-30\,\mathrm{dB}$, $\beta_\ell = 3$, and $\beta_d = -50\,\mathrm{dB}$. Figures 7(c)~7(e) in the second row are the formatted 3-D images, while Figures 7(f)~7(h) in the third row are the superposition of the 3-D image and the CAD model of target. All three methods produce satisfactory 3D images. The position of the voxels indicates the structural shape of the target and provides visual information about the target. The differences in the amplitudes of the voxels are too slight to be easily detected.

Figures 7(c) and 7(f) show the 3-D imaging result of our basic method. In this case, the sparse-imaging task is reduced to $M \times N^* = 10530 \times 4993$ dimensional, which is 0.43% of the dimensions of frequency-domain method. The proportion of nonzero elements of its dictionary is $\eta = 2.5\%$. In total, the data size of time-domain dictionary of basic method is only of the frequency-domain dictionary. In other words, it results in a savings of more than a factor of 9,300 in storage space. Moreover, the computation time of the solution is only 15.5 seconds. Figures 7(d) and 7(g) show the imaging result of the first improved time-domain method. The target separation was thresholded at $-25\,\mathrm{dB}$. The dimensions of the dictionary are reduced to $M^* \times N^* = 318 \times 4993$, less than 0.03% of the time-domain method. Its data size is only 1.84e-5 of the frequency domain dictionary. This results in more than a factor of 5.4e+4 storage savings. The solution took 2.4 seconds to compute. Figures 7(e) and 7(h) show the imaging results of the second improved time-domain method. In this case, the imaging task is divided into four lower-dimensional problems, which are $M_1^{**} \times N_1^{**} = 20 \times 711$, $M_2^{**} \times N_2^{**} = 41 \times 1083$, $M_3^{**} \times N_3^{**} = 25 \times 921$, $M_4^{**} \times N_4^{**} = 102 \times 2278$ dimensional, respectively. Both the data size and time complexity are considerably reduced.

An additional example is performed to show the applicability of our approach to distributed scattering centers. Figure 8(a) shows another three images with several distributed scattering centers of the SLICY target. The azimuth and elevation of the center are $\phi_{c,1} = -90°$, $\phi_{c,2} = -90°$, $\phi_{c,3} = -90°$, and $\theta_1 = 30°$, $\theta_2 = 33°$, $\theta_3 = 35°$. The aperture is $\widehat{\phi} = 5°$ degrees, and the azimuthal distance is

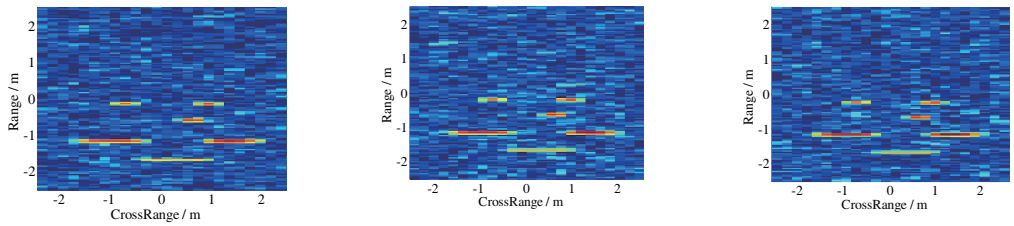

(a) Three SAR images of SLICY target at $\phi_{c,i} = -90°$

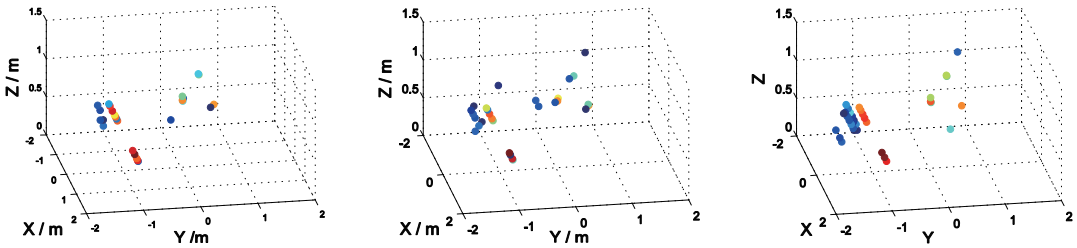

(b) Imaging result of basic method

(c) Imaging result of first improved method

(d) Imaging result of second improved method

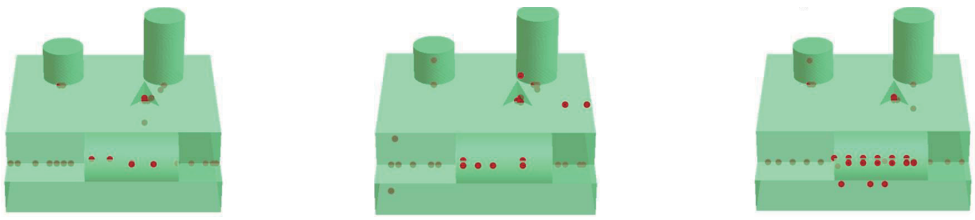

(e) The superposition of basic method

(f) The superposition of first improved method

(g) The superposition of second improved method

Figure 8. 3-D imaging results of three time-domain methods at azimuth $\phi = -90°$.

$\Delta\phi = 0.2^\circ$ degrees.

Figures 8(b)∼8(g) show the 3-D imaging results of our three time-domain methods with parameters $\beta_s = -25\,\text{dB}$, $\beta_\ell = 3$, and $\beta_d = -50\,\text{dB}$. The meaning of the subgraph is the same as in Figure 7. The image generated by the basic method is shown in Figures 8(b) and 8(e). In this example, the dimensions of sparse dictionary are $M \times N^* = 10530 \times 4763$, which is 0.42% of the frequency-domain dictionary. The percentage of nonzero elements in the time-domain dictionary is also $\eta = 2.5\%$, and the dictionary has only 1.06e-4 data size compared to the frequency-domain dictionary. Figures 8(c) and 8(f) show the result of the first improved method. The target separation is thresholded at $-25\,\text{dB}$. The dimensions of the sparse dictionary are reduced to $M^* \times N^* = 3329 \times 4763$, about 0.13% of the transitional methods. Some minor lobes appear and are caused by the truncation of the signal. Figures 8(d) and 8(g) show the imaging result of the second improved method. In this trial, the imaging model is divided into six sub-models with lower dimensions, which respectively are $M_1^{**} \times N_1^{**} = 168 \times 1365$, $M_2^{**} \times N_2^{**} = 187 \times 1286$, $M_3^{**} \times N_3^{**} = 65 \times 476$, $M_4^{**} \times N_4^{**} = 69 \times 598$, $M_5^{**} \times N_5^{**} = 83 \times 426$, $M_6^{**} \times N_6^{**} = 177 \times 945$.

7. CONCLUSIONS

In this paper, we present a basic approach and two improvements based on a time-domain sparse representation framework for 3D imaging from multi-view SAR data of a target. The proposed method exploits the properties of scattering physics in the time domain, including the geometric projection of 3-D and 2-D images, the information demonstrated by 2-D images, and the properties of 2-D time-domain responses, to improve the efficiency of 3-D imaging of targets. The basic approach is to reduce the column dimension and make the dictionary a sparse matrix. The first extension reduces both row and column dimensions. They are three to five orders of magnitude lower than frequency-domain methods in terms of storage and computation. The second extension decomposes the high-dimensional problem into a set of low-dimensional problems, which further improves the efficiency in certain cases. Roughly speaking, the proposed time-domain approach significantly reduces the dimension and data size of sparse representations compared to the traditional frequency-domain approach, which is also beneficial for solution efficiency improvement. Experimental results show that the proposed method effectively and efficiently generates high-resolution 3D images of the target, while reducing the daunting dimensionality and huge computational burden of the dictionary.

ACKNOWLEDGMENT

Financial support: The National Natural Science Foundation of China (62001486).

REFERENCES

1. Knaell, K., "Three-dimensional SAR from curvilinear apertures," *Proceedings of SPIE 2230, Algorithms for Synthetic Aperture Radar Imagery*, Orlando, FL, USA, 1994.
2. Soumekh, M., "Reconnaissance with slant plane circular SAR imaging," *IEEE Transactions on Image Processing*, Vol. 5, No. 8, 1252–1265, 1996.
3. Bryant, M. L., L. Gostin, and M. Soumekh, "3D E-CSAR Imaging of a T72 tank and synthesis of its SAR reconstructions," *IEEE Transactions on Aerospace and Electronic Systems*, Vol. 39, No. 1, 211–227, 2003.
4. Reigber, A. and A. Moreira, "First demonstration of airborne SAR tomography using multi-baseline L-band data," *IEEE Transactions on Geoscience and Remote Sensing*, Vol. 38, No. 5, 2142–2152, Sep. 2000.
5. Dungan, K. E. and L. C. Potter, "3D imaging of vehicles using wide aperture radar," *IEEE Transactions Aerospace and Electronic Systems*, Vol. 47, No. 1, 187–200, Jan.2011.
6. Zhou, J., Z. Shi, and Q. Fu, "Three-dimensional scattering center extraction based on wide aperture data at a single elevation," *IEEE Transactions Antennas Propagation*, Vol. 53, No. 3, 2051–2060, Mar. 2015.

7. Ertin, E., R. L. Moses, L. C. Potter, C. D. Austin, and S. Sharma., "GOTCHA experience report: Three-dimensional SAR imaging with complete circular apertures," *Algorithms for Synthetic Aperture Radar Imagery XIV, SPIE Defense and Security Symposium*, Apr. 9–13, 2007.
8. Richards, J. A., A. S. Willsky, et al., "Expectation-maximization approach to target model generation from multiple synthetic aperture radar images," *Optical Engineering*, Vol. 41, No. 1, 150–166, 2002.
9. Jackson, J. A. and R. L. Moses, "An algorithm for 3D target scatterer feature estimation from sparse SAR apertures," *Algorithms for Synthetic Aperture Radar Imagery XVI, SPIE*, 2009.
10. Jackson, J. A. and R. L. Moses, "Synthetic aperture radar 3D feature extraction for arbitrary flight paths," *IEEE Transactions on Aerospace and Electronic Systems*, Vol. 48, No. 3, 2065–2083, 2012.
11. Homer, J., I. D. Longstaff, Z. She, et al., "High resolution 3D imaging via multi-pass SAR," *IET Radar Sonar and Navigation*, Vol. 149, No. 1, 45–50, Feb. 2002.
12. Rigling, B. D. and R. L. Moses, "Three-dimensional surface reconstruction from multi-static SAR images," *IEEE Transactions on Image Processing*, Vol. 14, No. 8, 1159–1171, Aug. 2003.
13. Fornaro, G., F. Serafino, and F. Soldovieri, "Three-dimensional focusing with multipass SAR data," *IEEE Transactions on Geoscience and Remote Sensing*, Vol. 41, No. 3, 507–517, Mar. 2003.
14. Ertin, E., R. L. Moses, and L. C. Potter, "Interferometric methods for 3D target reconstruction with multi-pass circular SAR," *IET Radar, Sonar and Navigation*, Vol. 4, No. 3, 464–473, Jun. 2010.
15. Potter, L. C., E. Eritin, J. T. Parke, and M. Cetin, "Sparsity and compressed sensing in radar imaging," *Proceedings of the IEEE*, Vol. 98, No. 6, 1006–1020, Jun. 2010.
16. Samadi, S., M. Çetin, and M. A. Masnadi-Shirazi, "Sparse representation-based synthetic aperture radar imaging," *IET Radar Sonar and Navigation*, Vol. 5, No. 2, 182–193, Feb. 2011.
17. Herman, M. A. and T. Strohmer, "High-resolution radar via compressed sensing," *IEEE Transactions on Signal Processing*, Vol. 57, No. 6, 2275–2284, Jun. 2009.
18. Wei, Q., J. X. Zhou, H. Z. Zhao, and Q. Fu., "Three-dimensional sparse turntable microwave imaging based on compressive sensing," *IEEE Geoscience and Remote Sensing Letters*, Vol. 12, No. 4, 826–830, Apr. 2015.
19. Wu, C., Z. Zhang, and W. Yu, "Fast two-dimensional sparse signal gridless recovery algorithm for MIMO array SAR 3-D imaging," *IET Radar, Sonar & Navigation*, Vol. 14, No. 9, 1370–1381, 2020.
20. Wang, R., B. Deng, Y. Qin, and H. Wang, "Bistatic terahertz radar azimuth-elevation imaging based on compressed sensing," *IEEE Transactions on Terahertz Science and Technology*, Vol. 4, No. 6, 702–713, Nov. 2014.
21. Xu, G., M. Xing, X. Xia, L. Zhang, Y. Liu, and Z. Bao, "Sparse regularization of interferometric phase and aamplitude for InSAR image formation based on Bayesian representation," *IEEE Transactions on Geoscience and Remote Sensing*, Vol. 53, No. 4, 2123–2136, Apr. 2015.
22. Austin, C. D., E. Ertin, and R. L. Moses, "Sparse signal methods for 3-D radar imaging," *IEEE Journal of Selected Topics in Signal Processing*, Vol. 5, No. 3, 408–423, Jun. 2011.
23. Kajbaf, H., J. T. Case, Z. Yang, and Y. R. Zheng, "Compressed sensing for SAR-based wideband three-dimensional microwave imaging system using non-uniform fast fourier transform," *IET Radar Sonar and Navigation*, Vol. 7, No. 6, 658–670, Jul. 2013.
24. Qiu, W., J. Zhou, H. Zhao, and Q. Fu, "Fast sparse reconstruction algorithm for multidimensional signals," *Electronics Letters*, Vol. 50, No. 22, 1583–1585, Oct. 2014.
25. Qiu, W., J. zhou, Q. Fu, "Tensor representation for three-dimensional radar target imaging with sparsely sampled data," *IEEE Transactions on Computational Imaging*, Vol. 6, 263–275, 2019.
26. Zhu, X. X. and B. Richard, "Tomographic SAR inversion by-norm regularization-the compressive sensing approach," *IEEE Transactions on Geoscience and Remote Sensing*, Vol. 48, No. 10, 3839–3846, Oct. 2010.
27. Kim, S. J., K. Koh, M. Lustig, and S. Boyd, "A method for large-scale l1-regularized least squares," *IEEE Journal on Selected Topics in Signal Processing*, Vol. 1, No. 4, 606–617, Aug. 2007.

28. Mayhan, J. T., M. L. Burrows, K. M. Cuomo, and J. E. Piou, "High-resolution 3D snapshot ISAR imaging and feature extraction," *IEEE Transactions on Aerospace and Electronic Systems*, Vol. 37, No. 2, 630–641, Apr. 2001.
29. Goel, K. and A. Nico, "Three-dimensional positioning of point scatterers based on radargrammetry," *IEEE Transactions on Geoscience and Remote Sensing*, Vol. 50, No. 6, 2355–2363, Jun. 2012.
30. Richards, J. A., A. S. Willsky, and J. W. Fisher, "Expectation-maximization approach to target model generation from multiple synthetic aperture radar images," *Optical Engineering*, Vol. 41, No. 1, 150–166, Jan. 2002.
31. Thompson, P., M. Nannini, and R. Scheiber, "Target separation in SAR image with the MUSIC algorithm," *IEEE International Geoscience and Remote Sensing Symposium*, 468–471, 2007.
32. Liu, B., H. Wang, K. Wang, et al., "A foreground/fackground separation framework for interpreting polarimetric SAR images," *IEEE Geoscience and Remote Sensing Letters*, Vol. 8, No. 2, 288–292, Mar. 2011.
33. Davidson, G. and K. Ouchi, "Segmentation of SAR images using multitemporal information," *IET Radar Sonar and Navigation*, Vol. 150, No. 5, 367–374, Oct. 2003.
34. Koets, M. A. and R. L. Moses, "Image domain feature extraction from synthetic aperture imagery," *IEEE International Conference on Acoustics, Speech, and Signal Processing*, 2319–2322, 1999.
35. "*l*1_*ls*: Simple matlab solver for l1-regularized least squares problems," available at http://web.stanford.edu/∼boyd/l1_ls/.
36. Potter, L. C., D. M. Chiang, R. Carriere, and M. J. Gerry, "A GTD-based parametric model for radar scattering," *IEEE Transactions on Antennas and Propagation*, Vo. 43, No. 11, 1058–1067, Oct. 1995.
37. Batu, Ö. and M. Çetin, "Hyper-parameter selection in non-quadratic regularization-based radar image formation," *Proc. Algorithms for Synthetic Aperture Radar Imagery XV. SPIE Defense and Security Symp.*, Orlando, FL, Mar. 17–20, 2008.
38. Austin, C. R. Moses, J. Ash, and E. Ertin, "On the relation between sparse reconstruction and parameter estimation with model order selection," *IEEE Journal of Selected Topics in Signal Processing*, Vol. 4, No. 3, 560–570, Jun. 2010.